RMetS
Royal Meteorological Society

Eddy kinetic energy redistribution within windstorms *Klaus* and *Friedhelm*

G. Rivière,[a]* P. Arbogast[b] and A. Joly[b]
[a]*Laboratoire de Météorologie Dynamique/IPSL, Ecole Normale Supérieure/CNRS/UPMC, Paris, France*
[b]*CNRM/GAME, Météo-France/CNRS, Toulouse, France*

*Correspondence to: G. Rivière, LMD/IPSL, Ecole Normale Supérieure, 24 rue Lhomond, 75005 Paris, France.
E-mail: griviere@lmd.ens.fr

The formation of lower-tropospheric wind speed maxima is analyzed during the mature stage of two distinct windstorms using ERA-Interim reanalysis datasets and performing an eddy kinetic energy (EKE) budget. Both storms developed according to the Shapiro–Keyser conceptual model and crossed the large-scale low-frequency jet from its warm-air towards its cold-air side. The formation of strong wind regions are shown to depend on the position of the storms relative to the large-scale jet axis, which confirm theoretical results of a companion study. As long as the storms are travelling south of the low-frequency jet or close to the jet axis, the most intense EKE maxima as well as the total kinetic energy maxima are located in the warm sector of the surface cyclones on their southeastern side. As soon as the surface cyclones move to the north of the low-frequency jet, EKE is cyclonically redistributed in the lower troposphere, first to the northnorthwest of the cyclone's centre, and then to the southwest along the bent-back warm fronts. At this later stage, EKE, which is generated by baroclinic conversion in the mid-troposphere, is redistributed downwards by the vertical ageostrophic geopotential fluxes before being further redistributed southwestwards in the lower troposphere by the ageostrophic geopotential fluxes. This EKE redistribution led to the formation of a low-level westerly jet to the south of each cyclone centre behind the cold front. These common features between the two storms happened in spite of differences in their shape and environment.

Key Words: eddy kinetic energy; windstorms; jet crossing

Received 26 February 2014; Revised 13 June 2014; Accepted 17 June 2014; Published online in Wiley Online Library

1. Introduction

Because of the strong socio-economic impacts of surface damaging winds created by extratropical storms, and because of the difficulties encountered by forecasters in estimating their intensity, it is particularly important to improve our knowledge about their formation. Damaging surface winds are generally closely related to lower-tropospheric strong wind regions in the vicinity of fronts. These regions are often subjected to the formation of low-level jets in connection with the so-called conveyor belts (Harrold, 1973; Carlson, 1980; Schultz, 2001). Conveyor belts refer to the Lagrangian evolution of different air masses within extratropical cyclones. It is well known that the warm conveyor belt located in the warm sector ahead of a cold front corresponds to a southwesterly jet producing moderately strong winds (Browning and Pardoe, 1973; Lackmann, 2002; Clark *et al.*, 2005). These are the regions with the strongest wind speeds at the onset of a developing cyclone (e.g. Figure 1 in Sanders and Gyakum, 1980; Figure 4 in Grønas, 1995; Figure 5a in Wernli, 1997; Figure 12 in Nielsen and Sass, 2003; Figure 2a in Schultz and Sienkiewicz, 2013). Later on, during the frontal T-bone stage of Shapiro and Keyser (1990)'s cyclones, the bent-back warm front or cold-conveyor-belt jet intensifies creating strong northeasterlies around the top of the boundary layer (e.g. Figures 11 and 17 in Neiman *et al.*, 1993; Figure 9a in Rossa *et al.*, 2000). At the end of the wrapping of the bent-back warm front, during the seclusion of the warm air, the strongest wind speeds are observed ahead of the bent-back warm front on the southern side of the seclusion low (Grønas, 1995; Nielsen and Sass, 2003; Browning, 2004). Such a formation of very intense winds was already well known by meteorologists of the Bergen School and Norwegian forecasters and was called 'the poisonous tail of the bent-back occlusion' (Grønas, 1995). The strongest wind speeds south of the cyclone centre are not systematically related to the cold-conveyor-belt jet but can be due to the occurrence of sting jets (Smart and Browning, 2013; Martínez-Alvarado *et al.*, 2014). Sting jets refer to short-lived mesoscale descending airstreams at the tip of the cloud head leading to very strong horizontal winds at the top of the boundary layer and a downward transfer of their momentum that creates damaging winds at the surface (Browning, 2004). Martínez-Alvarado *et al.* (2012) showed that about one third of the most intense North Atlantic winter cyclones satisfy conditions for sting jet. It is not yet clear whether sting jets systematically occur in a Shapiro–Keyser

type cyclone (Gray *et al.*, 2011; Baker *et al.*, 2014). The answer depends probably on which criteria are used to identify sting jets. Idealized simulations of sting jets were performed by Baker *et al.* (2014) who showed that the descending air streams in the frontal fracture region, resulting in strong winds near the top of the boundary layer, are rather easy to obtain. However, the downward transfer of momentum from above the boundary layer to the surface is more difficult to simulate. To conclude, the formation of strong winds south of the cyclone centre in its later stage of development is an important topic which is still a matter of debate.

Motivated by such a context, the present article aims at providing a dynamical interpretation of the formation of low-level jets in real windstorms from an energy perspective. Our objective is not to describe wind formation at very small scales such as tens of kilometres but rather to provide a rationale for the kinetic energy distribution at spatial scales of hundreds of kilometres and to show how this energy distribution depends on the large-scale environmental flow in which the surface cyclone is embedded. The key role played by the large-scale environment on the shape and frontal structures of cyclones is already well established (Davies *et al.*, 1991; Schultz *et al.*, 1998; Wernli *et al.*, 1998). The new approach looks at the effect of the large-scale flow on the wind speed formation in the lower troposphere rather than on the fronts themselves. Besides, while the previously cited studies considered cyclones moving in the same environment, in this study cyclones travel in distinct environments and move from the warm-air to cold-air side of the large-scale jet.

In a companion article (Rivière *et al.*, 2014, hereafter denoted as RAJ14), an eddy kinetic energy (EKE) budget has been performed at the lower layer of a two-layer quasi-geostrophic model to systematically analyze the formation of kinetic energy maxima within idealized extratropical cyclones. As long as a cyclone moves on the warm-air side of the large-scale jet, the most intense EKE maxima, together with the total kinetic energy maxima, appear on the southeastern side of the cyclone. As soon as the cyclone crosses the jet axis, EKE is rapidly cyclonically redistributed and gets high values to the westsouthwest of the cyclone centre. This cyclonic redistribution of EKE on the cyclonic side of the large-scale jet is triggered by the convergence of the ageostrophic geopotential fluxes and the nonlinear advection. This leads to the formation of a low-level westerly jet, south of the cyclone during its later stage of evolution, which is consistent with the recent findings of Papritz and Schemm (2013) who used a dry version of a numerical weather prediction model. In other words, the same energy fluxes responsible for the so-called downstream development at upper levels (Orlanski and Katzfey, 1991; Chang and Orlanski, 1993; Orlanski and Sheldon, 1995) were shown to play a key role in the rearward and cyclonic redistribution of kinetic energy at low levels. This new energy interpretation of the low-level jet formation along the bent-back warm front in the Shapiro–Keyser type cyclone will be confirmed in the present real storm study.

Two European windstorms are analyzed in the present article using reanalysis datasets. First, the storm called *Klaus* (22–24 January 2009; Liberato *et al.*, 2011) caused serious damages in southwest France and northern Spain on 24 January 2009, killing six people in France and 17 in Spain. Its strength was particularly unusual with exceptional gusts reaching $45\,\mathrm{m\,s^{-1}}$ along the French Atlantic coast to the south of the sea level pressure minimum. In that region, Meteosat infrared images revealed the existence of multiple bands of cold dry air within the cloud head similar to sting jet properties. Similarly, the storm *Friedhelm* (7–9 December 2011; Baker *et al.*, 2013) produced high wind speeds to the south of the sea level pressure minimum over Scotland associated with both cold conveyor belt and sting jet air streams (Martínez-Alvarado *et al.*, 2014). It was also the most intense deepening extratropical cyclone observed during the DIAMET (DIAbatic influences on Mesoscale structures in ExtraTropical storms) field campaign (Vaughan *et al.*, 2014). Both storms crossed the large-scale mean jet from its warm-air to its cold-air side. *Klaus* was initiated far south of the jet while *Friedhelm* was formed much closer to the jet axis. These characteristics are relevant to the purpose of the present article as we want to demonstrate that the EKE redistribution processes are strongly dependent on the sign of the background horizontal shear, and in particular on the position of the cyclone relative to the mean jet axis. Therefore, *Klaus* and *Friedhelm* are good candidates for our study and will be compared with the idealized jet-crossing cyclone of RAJ14.

The article is organized as follows. Section 2 describes the dataset, the separation of the flow into high- and low-frequency parts and the EKE budget. Section 3 is dedicated to the description of the main characteristics of both storms before detailing the energy budget. The conclusion will be found in section 4.

2. Methodology

2.1. Data

The dataset used in the present study is provided by the ERA-Interim reanalysis project (Dee *et al.*, 2011). Forecast datasets starting at 0000 and 1200 UTC each day have been extracted with 3 h time steps. The advantage of the 3 h forecast datasets compared to the 6 h reanalysis datasets relies on the shorter time steps which allow a more accurate quantification of kinetic energy variations within rapidly changing extratropical cyclones. All meteorological variables have been extracted on a 0.75° latitude–longitude regular grid with a 50 hPa vertical spacing from 1000 to 100 hPa. As the various energy terms have been computed using horizontal and vertical finite-difference schemes, other grids have been also tested. The 0.5° grid gave similar results to the one used in the present study while the 1.5° grid provided less accurate estimation of the various EKE tendencies. However, the use of a 100 hPa vertical spacing gave very similar results as the 50 hPa vertical spacing. A 65-point temporal filter with a Gaussian shape and a 8-day cut-off period is applied to the 3 h dataset in order to separate the flow into high- and low-frequency parts. Therefore, to compute the high-frequency (or eddy or perturbation) and the low-frequency (or mean) field at each time, eight consecutive days centred on the time of interest were needed. For *Klaus*, datasets were thus extracted from 18 to 28 January 2009 and for *Friedhelm* from 2 to 12 December 2011.

2.2. EKE budget

The primes and bars represent respectively high-pass and low-pass operators and the sum of the high- and low-frequency components is equal to the total flow. The perturbation momentum equations can be obtained by applying the high-pass filter to the primitive momentum equations in isobaric coordinates:

$$\frac{\partial}{\partial t}\mathbf{u}' + (\mathbf{u}_3\cdot\nabla_3\mathbf{u})' = -f\mathbf{k}\times\mathbf{u}' - \nabla\Phi' + \mathbf{F}', \qquad (1)$$

where Φ is the geopotential, $\mathbf{k}$ the vertical unit vector, $\mathbf{u}_3$ the three-dimensional velocity vector, f the Coriolis parameter and $\mathbf{u}$ the horizontal velocity vector. ∇ and ∇_3 are respectively the horizontal and three-dimensional gradient operators in isobaric coordinates ($\nabla_3 = \nabla + \mathbf{k}\partial/\partial p$). Viscous forces are represented by $\mathbf{F}$. Then, by multiplying the previous equation by the high-frequency velocity, we obtain the equation for the high-frequency EKE (Orlanski and Katzfey, 1991; Rivière and Joly, 2006):

$$\frac{\partial}{\partial t}K' = -\mathbf{u}'\cdot(\mathbf{u}_3\cdot\nabla_3\mathbf{u})' - \mathbf{u}'\cdot\nabla\Phi' + \mathbf{u}'\cdot\mathbf{F}', \qquad (2)$$

where $K' \equiv 0.5\mathbf{u}'^2$ is the high-frequency EKE. Since our study focuses on EKE redistribution around the surface cyclone, it is

more suitable to introduce the phase speed of the surface cyclone (denoted as **c**) and to analyze the EKE evolution in the cyclone frame of reference as follows:

$$\frac{\mathrm{D}}{\mathrm{D}t}K' = -\mathbf{u}'\cdot(\mathbf{u}_3\cdot\nabla_3\mathbf{u})' + \mathbf{c}\cdot\nabla K' - \mathbf{u}'\cdot\nabla\Phi' + \mathbf{u}'\cdot\mathbf{F}', \qquad (3)$$

where $\mathrm{D}/\mathrm{D}t = \partial/\partial t + \mathbf{c}\cdot\nabla$ is the time operator in the cyclone frame of reference. The sum of the first two terms on the r.h.s. of Eq. (3) can be expressed as

$$\begin{aligned} &-\mathbf{u}'\cdot(\mathbf{u}_3\cdot\nabla_3\mathbf{u})' + \mathbf{c}\cdot\nabla K' \\ &\quad = (\mathbf{c}-\overline{\mathbf{u}}_3)\cdot\nabla_3 K' - \mathbf{u}'_3\cdot\nabla_3 K' - \mathbf{u}'\cdot(\mathbf{u}'_3\cdot\nabla_3\overline{\mathbf{u}}) \\ &\qquad - \mathbf{u}'\cdot(\overline{\mathbf{u}}_3\cdot\nabla_3\overline{\mathbf{u}}) + \mathbf{u}'\cdot\overline{(\mathbf{u}_3\cdot\nabla_3\mathbf{u})}. \end{aligned} \qquad (4)$$

The first term on the r.h.s. of Eq. (4), $\mathrm{ADVLIN} = (\mathbf{c}-\overline{\mathbf{u}}_3)\cdot\nabla_3 K'$, is called the linear advection term because it contains the advection of EKE by the mean flow but also includes the adjustment term $\mathbf{c}\cdot\nabla K'$ to stay in the cyclone frame of reference. The second term, $\mathrm{ADVNL} = -\mathbf{u}'_3\cdot\nabla_3 K'$, is called the nonlinear advection term because it contains the advection of EKE by the perturbation velocity. The third term, $\mathrm{REY} = -\mathbf{u}'\cdot(\mathbf{u}'_3\cdot\nabla_3\overline{\mathbf{u}})$, is the Reynolds stress term which is reduced in quasi-geostrophic dynamics to the barotropic conversion rate from EKE to mean kinetic energy (the next section gives its formulation in primitive equations). The final terms, $\mathrm{RES} = -\mathbf{u}'\cdot(\overline{\mathbf{u}}_3\cdot\nabla_3\overline{\mathbf{u}}) + \mathbf{u}'\cdot\overline{(\mathbf{u}_3\cdot\nabla_3\mathbf{u})}$, are called residual as they are small compared to the other terms. The pressure work $\mathrm{PWK} = -\mathbf{u}'\cdot\nabla\Phi'$ can be written as

$$-\mathbf{u}'\cdot\nabla\Phi' = \omega'\frac{\partial\Phi'}{\partial p} - \nabla(\Phi'\mathbf{u}'_{\mathrm{a}}) - \frac{\partial}{\partial p}(\omega'\Phi'), \qquad (5)$$

where the ageostrophic geopotential fluxes $\Phi'\mathbf{u}'_{\mathrm{a}}$ have been computed as in Orlanski and Sheldon (1995):

$$\Phi'\mathbf{u}'_{\mathrm{a}} = \Phi'\mathbf{u}' - \mathbf{k}\wedge\nabla\frac{\Phi'}{2f(y)}. \qquad (6)$$

The first term on the r.h.s. of Eq. (5), $\mathrm{CI} = \omega'\partial\Phi'/\partial p$, is the baroclinic internal conversion rate allowing the energy transfer from eddy potential energy to EKE. The second term, $\mathrm{FHAG} = -\nabla(\Phi'\mathbf{u}'_{\mathrm{a}})$, is the convergence of the horizontal ageostrophic geopotential fluxes and the third term, $\mathrm{FVAG} = -\partial(\omega'\Phi')/\partial p$, the convergence of the vertical ageostrophic geopotential fluxes. These last two terms redistribute EKE horizontally and vertically respectively. Finally note that Eq. (3) is very similar to Eq. 3.14 of Orlanski and Katzfey (1991), except that a low-frequency filter is used here. In the particular case where the bar denotes a time average as in Orlanski and Katzfey (1991), one can easily deduce that $\mathrm{RES} = \mathbf{u}'\cdot\overline{(\mathbf{u}'_3\cdot\nabla_3\mathbf{u}')}$ and our EKE equation becomes equal to that of Orlanski and Katzfey (1991).

Let us now briefly describe the computation of the different terms. The time and space derivatives are all computed with centred finite-difference schemes. The phase velocity **c** is obtained by computing the position of the high-frequency geopotential minimum at 900 hPa $\mathbf{x}_{\min}(t)$ and by using the 3 h finite-difference scheme $\mathbf{c} = \delta\mathbf{x}/\delta t$, where $\delta\mathbf{x}(t) = \mathbf{x}_{\min}(t+\delta t) - \mathbf{x}_{\min}(t-\delta t)$ and $\delta t = 3$ h. Equation (3) is approximated by the following scheme:

$$\begin{aligned} &\frac{K'(\mathbf{x}+\delta\mathbf{x}, t+\delta t) - K'(\mathbf{x}-\delta\mathbf{x}, t-\delta t)}{2\delta t} = \\ &\frac{1}{2}\frac{\mathrm{D}K'}{\mathrm{D}t}(\mathbf{x},t) + \frac{1}{4}\left\{\frac{\mathrm{D}K'}{\mathrm{D}t}(\mathbf{x}-\delta\mathbf{x},t-\delta t) + \frac{\mathrm{D}K'}{\mathrm{D}t}(\mathbf{x}+\delta\mathbf{x},t+\delta t)\right\}. \end{aligned} \qquad (7)$$

At each time t, the EKE tendencies are thus obtained by computing the terms on the r.h.s. of Eq. (3) at times $t-\delta t$, t, $t+\delta t$, by then projecting them in the cyclone frame of reference at time t and finally summing them using weights 1/4, 1/2 and 1/4 respectively. This weighting procedure has been shown to improve the accuracy of the energy budget.

Throughout this article, an EKE budget is made by averaging Eq. (3) between 650 and 850 hPa. The sum of the frictionless terms on the rhs of Eq. (3) are found to represent the correct EKE tendencies at these levels while below 850 hPa the dissipative processes of the boundary layer become important and diabatic terms should be included to close the EKE budget.

3. Results

3.1. Description of the real cases

Figure 1 shows that both cyclones crossed the mean jet axis from its warm-air to cold-air side with *Friedhelm* being initiated much closer to the jet axis than *Klaus*. The tendency for the cyclones to cross the mean flow axis can be viewed as a generalization in a midlatitude baroclinic context of the beta-drift mechanism (Gilet *et al.*, 2009; Rivière *et al.*, 2012). *Klaus* and *Friedhelm* travelled across the northeast Atlantic by interacting with an upper-level trough. In the early stages, the upper troughs were far upstream of the surface cyclones (Figure 1(a, b)). Then, as they neared the surface cyclones, they strongly amplified them (Figure 1(c, d)). At the end of their evolution, the upper-level vorticity maxima lay south of the surface cyclones (Figure 1(e)-(h)). These characteristics are typical of Type B cyclogenesis (Petterssen and Smebye, 1971). Another common feature of both storms can be found in the formation of a comma-shaped vorticity at a later stage (Figure 1(f, g)). Differences in the shape of the low-level vorticity are also noticeable. For instance, at the early stages, the low-level vorticity pattern of *Klaus* and its upper-level precursor were more elongated than their counterparts in the *Friedhelm* case (Figure 1(a, b)). This feature might partly come from the fact that *Klaus* and its upper-level trough moved on the anticyclonic-shear side of the jet while *Friedhelm* was much closer to the jet axis. It is also worth noting that the two upper-level low-frequency jets are drastically different. The *Klaus* jet is much wider than the *Friedhelm* jet (shadings). Finally, it is important to note that the comma-shaped vorticity or the spiral of vorticity was observed when the cyclones were already on the cyclonic-shear side of their respective low-frequency jet (Figure 1(f, g)).

Figure 2 shows the time evolution of the eddy, mean and total wind speed averaged between 650 and 850 hPa for *Klaus*. As long as the surface cyclone moved on the anticyclonic side of the low-level low-frequency jet, i.e between 0000 and 1200 UTC on 23 January, the maximum eddy wind speed was located to the southeast of the cyclone centre (Figure 2(a, c, e)). As soon as the surface cyclone entered into the cyclonic side of the mean jet, eddy wind speed maxima shifted, first to the north of the cyclone centre (Figure 2(g)) and then to the westsouthwest (Figure 2(i)). This displacement of strong perturbation wind regions relative to the cyclone centre has the following consequences on the evolution of the total wind speed maxima with time. Before the jet-crossing phase, i.e from 0000 to 1200 UTC on 23 January 2009, the total wind speed maxima were more or less at the same place as the eddy wind maxima, that is in the warm sector of the cyclone (Figure 2(b, d, f)), which is consistent with other observational studies (e.g. Grønas, 1995; Nielsen and Sass, 2003). In that region where the total wind speed reached its maximum, the eddy velocities were northeastward oriented along the direction of the cold front and the mean velocities were eastward oriented (see arrows). This zone of highest wind speeds has a southwest–northeast elongated structure parallel to the cold front (Figure 2(d, f)). At 1800 UTC on 23 January 2009, during the T-bone stage which is clearly visible in Figure 2(h), high total wind speeds were still ahead of the cold front. However, the maximum wind speed was found to be behind the cold front in a region where the eddy winds were weaker (Figure 2(g)) because the latter winds aligned favourably with the mean winds there. At this moment, the total wind speed maximum was not reached in

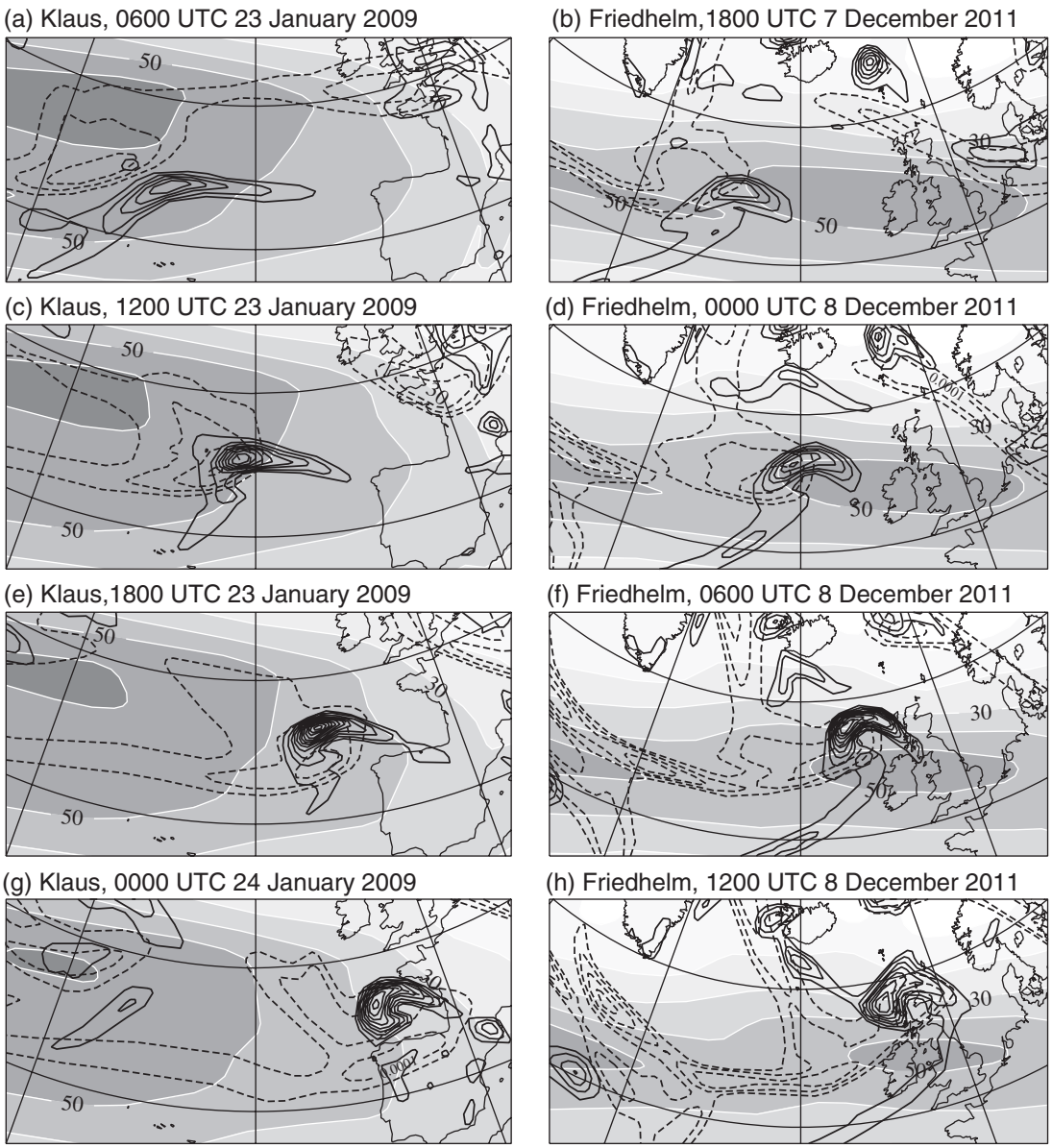

Figure 1. Time evolution of the high-frequency relative vorticity at 300 hPa (dashed black contours with interval $5 \times 10^{-5} s^{-1}$), 900 hPa (solid black contours with interval $5 \times 10^{-5} s^{-1}$) and the 300 hPa low-frequency wind speed (shading with interval 10 m s^{-1}) for (a, c, e, g) *Klaus* and (b, d, f, h) *Friedhelm*.

regions where the eddy wind speeds were the most intense, being located either to the east where the eddy and mean winds were almost perpendicular to each other, or to the north where both winds had the opposite orientation (Figure 2(g)). At 0000 UTC on 24 January 2009, i.e at the beginning of the seclusion stage, a large amount of eddy wind speed accumulated to the westsouthwest of the surface cyclone (Figure 2(i)). Because the eddy winds are strong and align favourably with the mean westerlies to the south of the cyclone centre, a strong low-level westerly jet was formed there during the seclusion process (Figure 2(j)).

The *Friedhelm* case brings similarities with the *Klaus* case (Figure 3). When the surface cyclone moved along the jet core, both the eddy and total wind speeds attained their maximum in the warm sector to the southeast of the cyclone centre in a region where the eddy winds were northeastward oriented (Figure 3(a)–(d)). Regions of highest eddy wind speeds lay on the southeastern side of the cyclone and extended from the southwest to the northeast. This situation corresponds to the time when *Klaus* was moving along the jet axis as well (Figure 2(c)–(f)). Later on, when *Friedhelm* moved further north, away from the jet core, the southwest–northeast elongated structure of the high eddy wind speed regions was lost (Figure 3(e)). There was a strong increase in eddy wind speeds northeast of the cyclone where the eddy winds were northwestward oriented, similar to *Klaus* in Figure 2(g). However, because of the more favourable configuration with the mean winds on the southeastern flank of the cyclone, the total wind speed maxima were still reached there to form a southwest–northeast jet parallel to the cold front (Figure 3(f)). During the T-bone stage and at the beginning of the seclusion process, the highest total wind speeds appeared both ahead of and behind the cold front, forming a zonally oriented jet perpendicular to the cold front (Figure 3(h)). The high total wind speeds behind the cold front result from a significant increase in eddy westerly winds to the southsouthwest of the cyclone (Figure 3(g)) which favourably align with the mean westerlies. This situation is similar to *Klaus* in Figure 2(i, j). At the end of the seclusion stage (Figure 3(i,j)), the maximum total wind speed was reached behind the cold front.

The different stages can be summarized as follows and can be illuminated at the light of RAJ14 results. As long as a surface cyclone travels on the anticyclonic side of the mean jet, the highest total wind speeds are southeast of the cyclone centre, ahead of the cold front, in regions where the northeastward eddy winds reach their maximum intensity. These features are interpreted as resulting from the presence of both the background anticyclonic shear and the background relative-vorticity gradient induced by the mean westerly jet (Figure 8(n) of RAJ14). A zone of high wind speeds parallel to the cold front is formed during this early stage. When the surface cyclone moves near the large-scale jet axis, its southwest–northeast elongation disappears and the eddy

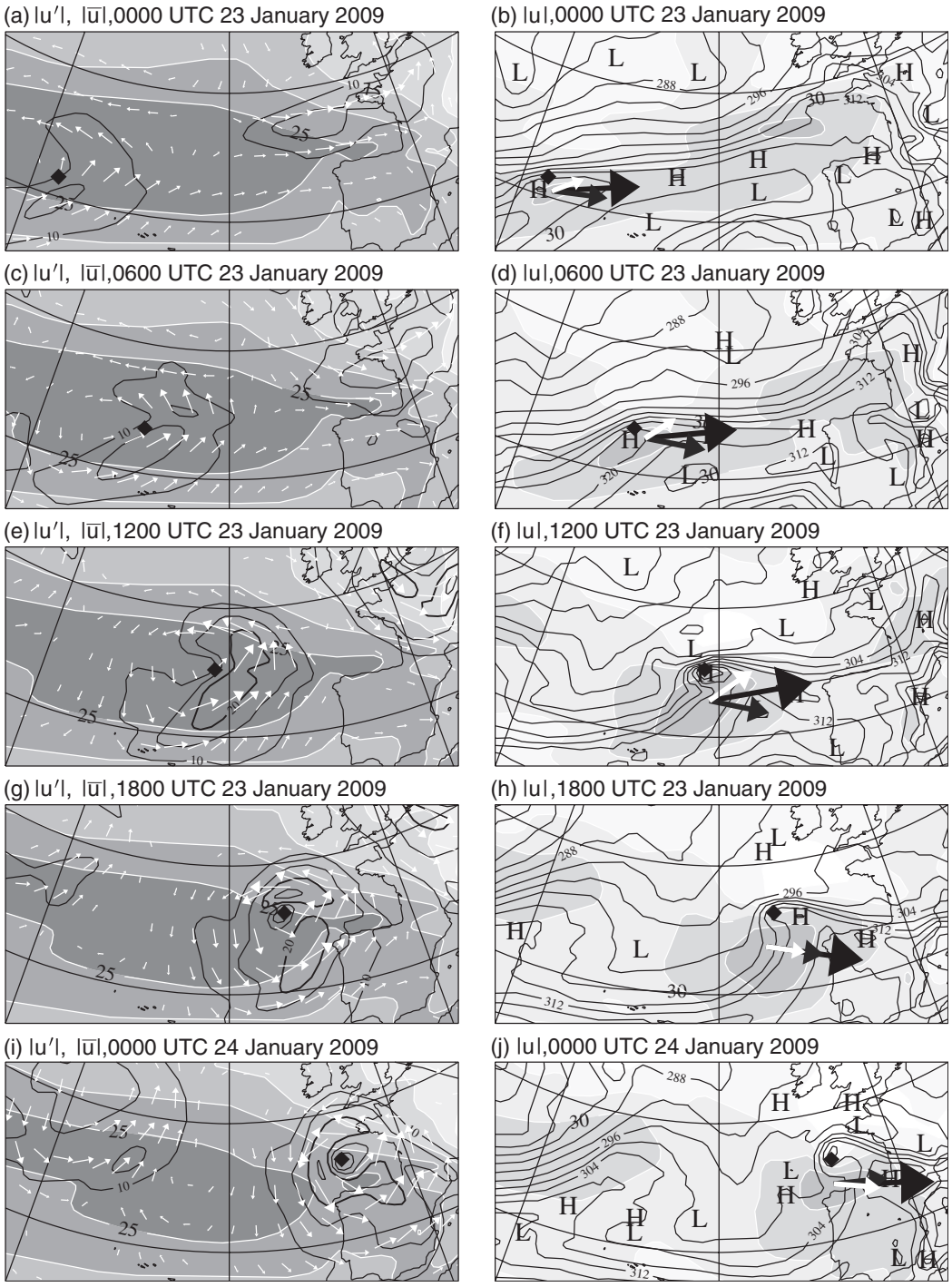

Figure 2. (a, c, e, g, i) Time evolution of the high-frequency winds (white arrows) and their magnitude (solid black contours with interval 5 m s^{-1}; the bold contour denotes 20 m s^{-1}) together with the magnitude of the low-frequency wind (shading with interval 5 m s^{-1}) for *Klaus*. The winds have been averaged between 650 and 850 hPa. (b, d, f, h, j) Time evolution of the magnitude of the total wind averaged between 650 and 850 hPa (shading with interval 10 m s^{-1}) and equivalent potential temperature at 900 hPa (black contours with interval 4 K). The white, grey and black arrows denote respectively the high-frequency, low-frequency and total wind velocities at the grid point of maximum total wind speed. In all panels, the black diamond denotes the minimum high-frequency geopotential at 900 hPa.

wind speeds intensify east of the cyclone centre, which can be explained by the strong background relative-vorticity gradient associated with the mean jet (e.g. Figure 9(j) of RAJ14). As soon as the cyclone moves on the cyclonic side of the mean jet, eddy wind speed maxima are cyclonically displaced, first in regions where they do not combine favourably with the mean winds (i.e. to the east and north of the cyclone centre). During that stage, the total wind speeds have large amplitudes both ahead of and behind the cold front. Finally, once the cyclone is entirely embedded on the cyclonic side of the mean jet, the seclusion stage occurs and is characterized by a significant accumulation of EKE, west, southwest and south of the cyclone centre. This leads to the formation of a westerly jet behind the cold front, south of the cyclone centre, in a region where the eddy and mean winds favourably add to each other. These common features of *Klaus* and *Friedhelm* compare well with the idealized jet-crossing cyclone of RAJ14 (their Figure 9, second column). Since strong wind regions can be interpreted from the spatial distribution of the eddy wind field relative to the mean flow, the rest of the article is dedicated to the understanding of the EKE budget.

3.2. *EKE budget*

Let us first analyze the EKE budget at 1200 UTC on 23 January when *Klaus* was crossing the mean jet (Figure 4). The diagnosed EKE tendency (i.e. the l.h.s. of Eq. (3)) is mainly positive and shows a global EKE increase (Figure 4(a)). The sum of the frictionless terms (i.e the r.h.s. of Eq. (3)) shown in Figure 4(b)

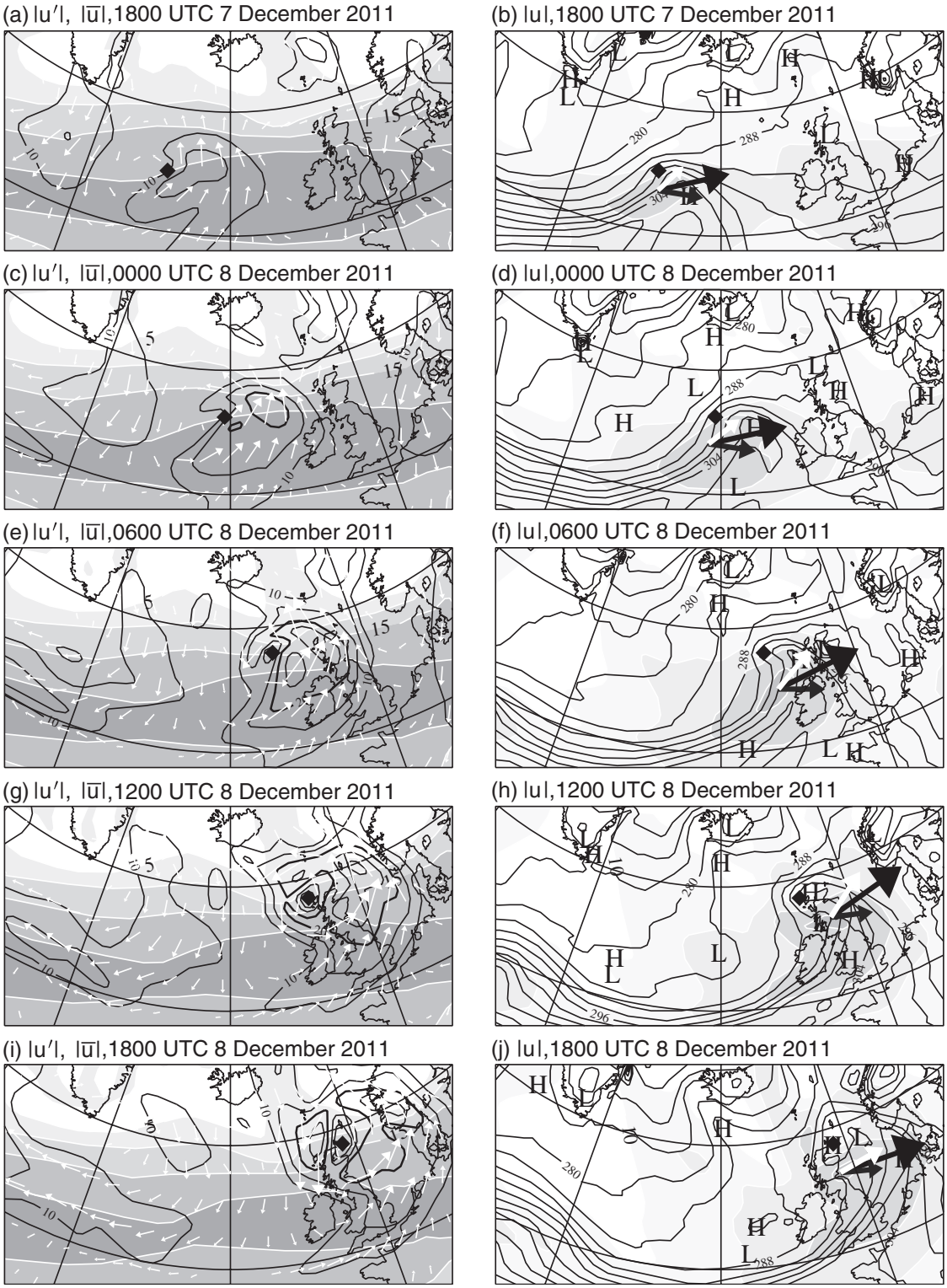

Figure 3. As Figure 2, but for *Friedhelm*.

correctly represents the structure of the EKE tendency as EKE increases southeast and northeast of the cyclone centre. However, the negative tendencies on the southwestern side of the cyclone are overestimated. The sum of the frictionless terms is then decomposed into the pressure work and the rest of the terms (i.e. Reynolds stress plus advection) in Figure 4(d, e). Even though PWK presents both positive and negative tendencies, the positive values cover a larger area than the negative ones. It is less true for (REY + ADV + RES) which roughly shows as many positive as negative values. Therefore, the global increase in EKE is mainly explained by the pressure work. Note also that PWK and (REY + ADV + RES) tend to strongly compensate each other which can be easily understood when considering simple idealized cases (Appendix).

The decomposition of the pressure work (Eq. (5)) into the baroclinic conversion rate CI, the convergence of the vertical ageostrophic geopotential fluxes FVAG and the convergence of the horizontal ageostrophic geopotential fluxes FHAG is shown in Figure 4(c, g, h). The redistribution terms FVAG and FHAG show negative values as large as positive ones whereas CI is positive over all regions and has large amplitudes on the eastern flank of the cyclone. This positive value of CI is a classical feature of the baroclinic interaction between a surface cyclone and an upper-level trough (e.g. Orlanski and Katzfey, 1991; Rivière and Joly, 2006). FVAG has stronger negative values than positive ones. This term is a sink of energy for the mid-to-low troposphere and has been already shown to attenuate the development of real surface cyclones (Rivière and Joly, 2006) and idealized ones

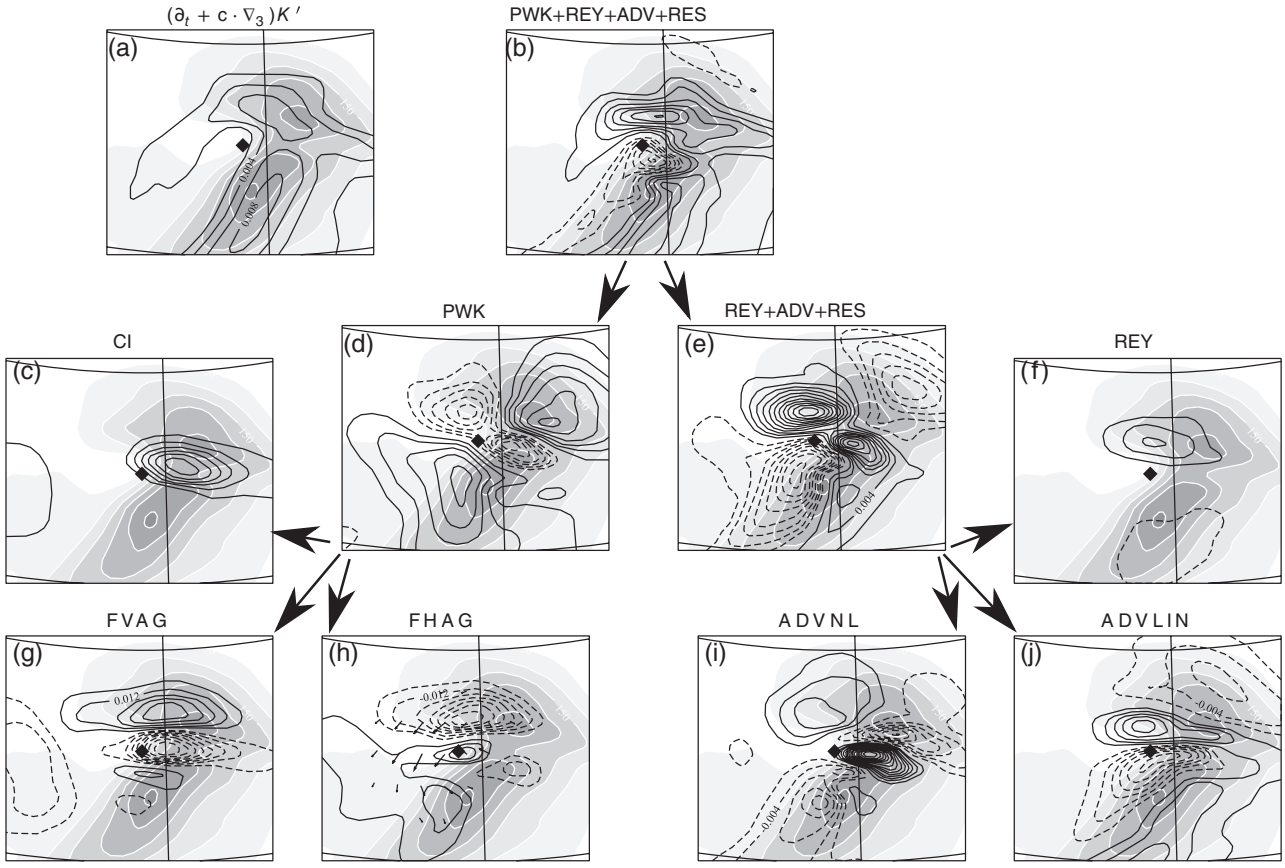

Figure 4. Eddy kinetic-energy budget averaged between 650 and 850 hPa for *Klaus* at 1200 UTC on 23 January. (a) Eddy kinetic energy tendency by following the surface cyclone ($(\partial_t + \mathbf{c} \cdot \nabla)K'$); (b) sum of the pressure work, advection and Reynolds stress terms; (c) baroclinic conversion from eddy potential energy to eddy kinetic energy CI; (d) pressure work PWK; (e) sum of the advection and Reynolds stress terms; (f) Reynolds stress term REY; (g) convergence of the vertical ageostrophic fluxes FVAG; (h) convergence of the horizontal ageostrophic fluxes FHAG; (i) nonlinear advection term ADVNL and (j) linear advection term ADVLIN. The contour interval is $2 \times 10^{-3} \mathrm{m^2 s^{-3}}$ with dashed and solid contours representing negative and positive values respectively, except for (c), (g) and (h) for which the contour interval is $6 \times 10^{-3} \mathrm{m^2 s^{-3}}$. The shadings represent the eddy kinetic energy with interval $50\,\mathrm{m^2 s^{-2}}$. The black diamond denotes the position of the minimum high-frequency geopotential at 900 hPa at the time of interest.

(Rivière *et al.*, 2013). Furthermore, this term may eventually favour a transient decay stage (Rivière and Joly, 2006). The negative values of FVAG to the extreme west of the domain are mainly due to descending motions upstream of the upper trough and an upward transfer of kinetic energy while the strong negative values to the northeast of the low centre are linked to ascending motions and a downward transfer of kinetic energy (Figure 3 of RAJ14). The negative FVAG values are closely related to the positive CI patterns. This reflects the fact that the conversion from eddy potential to EKE is rapidly redistributed upwards and downwards on the western and eastern sides respectively. The ageostrophic geopotential fluxes are southwestward oriented, redistribute EKE toward the southwestern regions of the cyclone but are rather weak in comparison with the later stages as hereafter shown.

The sum (REY + ADV + RES) is decomposed into the Reynolds stress term REY (Figure 4(f)), linear advection ADVLIN (Figure 4(j)) and nonlinear advection ADVNL (Figure 4(i)). The residue term RES (i.e the last terms in Eq. (4)) is very small compared to the other ones and will not be discussed here. Let us first interpret the Reynolds stress term by writing it as

$$-\mathbf{u}' \cdot (\mathbf{u}'_3 \cdot \nabla_3 \overline{\mathbf{u}}) = -\mathbf{u}' \cdot (\mathbf{u}' \cdot \nabla \overline{\mathbf{u}}) - \mathbf{u}' \cdot \left(\omega' \frac{\partial \overline{\mathbf{u}}}{\partial p} \right). \qquad (8)$$

The first term on the r.h.s. is the barotropic conversion rate from mean energy to EKE, while the second term is a baroclinic conversion rate from mean energy to EKE. In quasi-geostrophic dynamics, the Reynolds stress term is reduced to the former term. In the present case, the positive tendency of REY to the north (Figure 4(f)) is due to the baroclinic component while the barotropic one is rather small (not shown). The positive peak values of the baroclinic term to the north result from the correlation between the negative perturbation zonal wind and the negative perturbation omega velocity in presence of a positive vertical mean shear (Eq. (8)). Nonlinear advection is also an important term that tends to cyclonically redistribute EKE (Figure 4(i)). Around each EKE maximum, negative and positive tendencies appear upstream and downstream of the eddy streamlines respectively. The linear advection pattern of Figure 4(j) can be interpreted as follows. The vertical advection has been checked to be very small and the linear advection term can be reduced to ADVLIN $\simeq (\mathbf{c} - \overline{\mathbf{u}}) \cdot \nabla K'$. The zonal component of $\mathbf{c} - \overline{\mathbf{u}}$ is small around the cyclone as we are close to the steering level, i.e where the eastward phase velocity equals the mean zonal wind (Lim *et al.*, 1991). However, the meridional component of $\mathbf{c} - \overline{\mathbf{u}}$ is non-negligible and it is poleward-oriented because the surface cyclone crossed the mean flow axis from the south to the north. It leads to positive and negative tendencies on the equatorward and poleward flanks of each EKE maximum respectively as shown in Figure 4(j). Note finally that the northnorthwest positive tendency of (REY + ADV + RES) (Figure 4(e)) is the unique contributor to the positive tendency of (PWK + REY + ADV + RES) (Figure 4(b)) in that region. So it is the sum of the advection and of the Reynolds stress terms which contributes to initiate the cyclonic rolling-up of EKE on the northern side of the cyclone at that time.

At 0000 UTC 24 January, the diagnosed EKE tendency (i.e the lhs of Eq. (3)) is mainly positive to the southwest and negative to the northeast of the cyclone center (Figure 5(a)). The sum of the frictionless terms exhibits the same general tendency even though strong discrepancies exist over land (see over Spain in Figure 5(b)) probably because the friction terms are important there and tend to dissipate EKE. Despite these discrepancies,

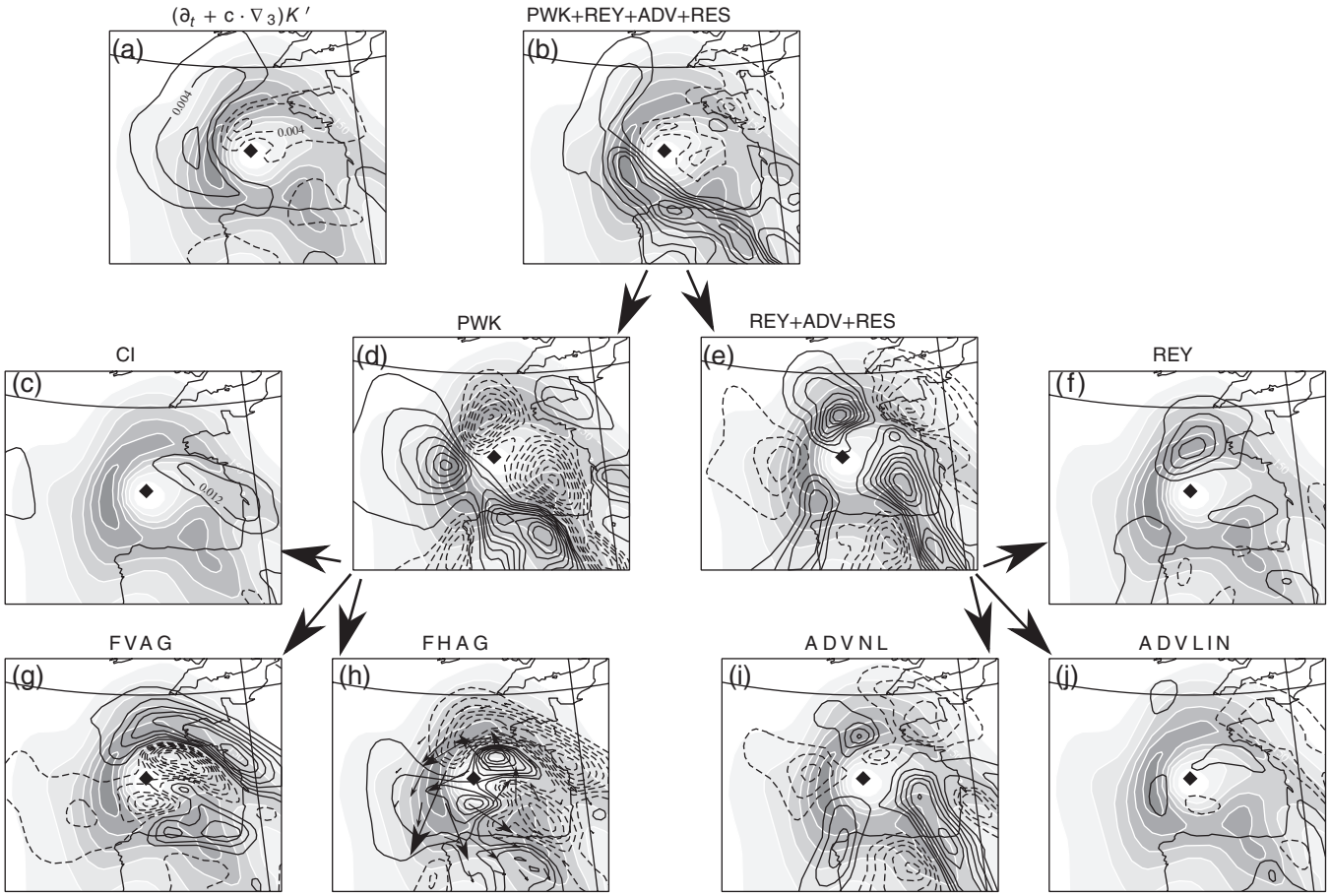

Figure 5. As Figure 4, but at 0000 UTC on 24 January 2009.

the EKE budget is satisfying for our purpose as the sum of the frictionless dynamical terms represents the cyclonic rolling-up of EKE around the cyclone center rather well. In particular, the EKE increase to the southwest, which is the key feature for the formation of the low-level jet to the south, is clearly reproduced by the frictionless terms. The pressure work is responsible for the main positive EKE tendencies in the southwestern quadrant of the low (Figure 5(d)) while the sum of the Reynolds stress and advection shows a dipolar anomaly tendency in the same quadrant (Figure 5(e)). The decomposition of the pressure work into CI, FVAG and FHAG clearly shows that the latter term is the major contributor to the positive values of PWK in the southwestern quadrant (Figure 5(c,g,h)). The horizontal ageostrophic geopotential fluxes converge there and redistribute EKE from the northeast to the southwest of the low. The decomposition of (REY + ADV + RES) shows that the dipolar anomaly tendency centred over the EKE maximum located in the southwestern quadrant is simply due to the nonlinear advection term (Figure 5(i)). The Reynolds stress term is mainly positive on the northern flank of the low which comes from its baroclinic part as 12 h before (Figure 5(f)). The linear advection term is now rather weak because the phase velocity is close to the mean flow velocity as the cyclone was moving along the jet on its northern side at this later stage (Figure 5(j)).

The *Friedhelm* scenario is rather similar to the *Klaus* one, even though there are some nuanced differences between the two. Figure 6 presents the EKE budget at the beginning of the seclusion stage. The estimated EKE tendency is, on average, positive, which means that the cyclone is still deepening during the seclusion stage (Figure 6(a)) and corresponds to the largest EKE increase of its life cycle (not shown). This is to be contrasted with *Klaus* which deepened more rapidly earlier during the T-bone stage. The EKE tendencies given by the sum of the frictionless terms agree well with the estimated EKE tendencies (Figure 6(a, b)). In particular, there is an EKE increase in the southwestern quadrant of *Friedhelm* which is clearly visible in both panels. Without any ambiguity, it is the pressure work that creates this positive tendency because the remaining terms (REY + ADV + RES) are negative in that particular quadrant (Figure 6(d, e)). By comparing Figure 6(c, g, h), we deduce that the convergence of the horizontal ageostrophic fluxes solely explains the positive tendency of PWK in that quadrant. The baroclinic conversion CI is strongly positive to the northeast and the convergence of the vertical ageostrophic fluxes FVAG is positive to the north and negative to the south. The sum of the latter terms is thus positive to the northeast and negative to the southwest but is entirely overwhelmed by the positive values of FHAG in the later part of the cyclone. In other words, the energy conversion and energy transfer from other vertical levels is horizontally redistributed by the horizontal ageostrophic fluxes from the northeast to the southwest in the lower troposphere. This is the same picture as that provided by the pressure work for *Klaus* at that particular stage, except that CI is much stronger in the *Friedhelm* case. The decomposition of the sum (REY + ADV + RES) is shown in Figure 6(f, i, j). The Reynolds stress term is positive to the northwest and southeast of the low centre, the former being due to the baroclinic component of REY as for *Klaus* and the latter being due to its barotropic component, that is the barotropic conversion (not shown). The nonlinear advection term plays a very minor role in the southwestern quadrant of the cyclone. The nonlinear advection term shows dipolar anomalies over each EKE maximum oriented along the direction of the perturbation wind which is particularly visible on the southeastern part of the low as EKE has a well-defined peak there. As for *Klaus*, $\mathbf{c} - \overline{\mathbf{u}}$ being mainly poleward oriented because of the poleward component of $\mathbf{c}$, the linear advection term exhibits poleward oriented dipolar anomalies centred over each EKE maximum (see the northern EKE maximum in Figure 6(j)).

To conclude on the EKE budgets in the lower troposphere, the sum of the frictionless terms is in good agreement with the estimated EKE tendencies. Common findings are found for *Klaus* and *Friedhelm*. At the early stages, the global increase in EKE is primarily due to the pressure work. Later in the evolution,

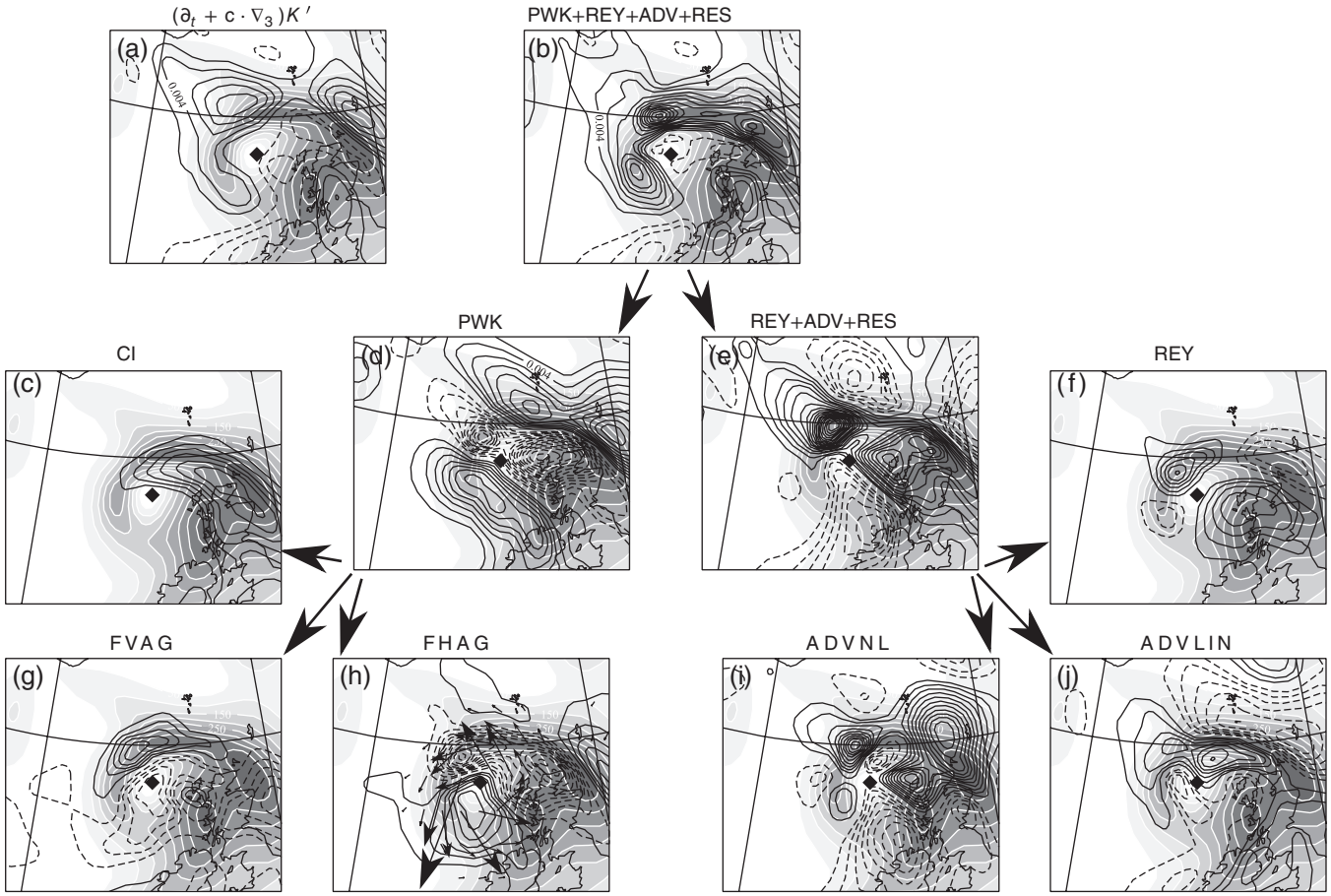

Figure 6. As Figure 4, but for *Friedhelm* at 0900 UTC on 8 December 2011.

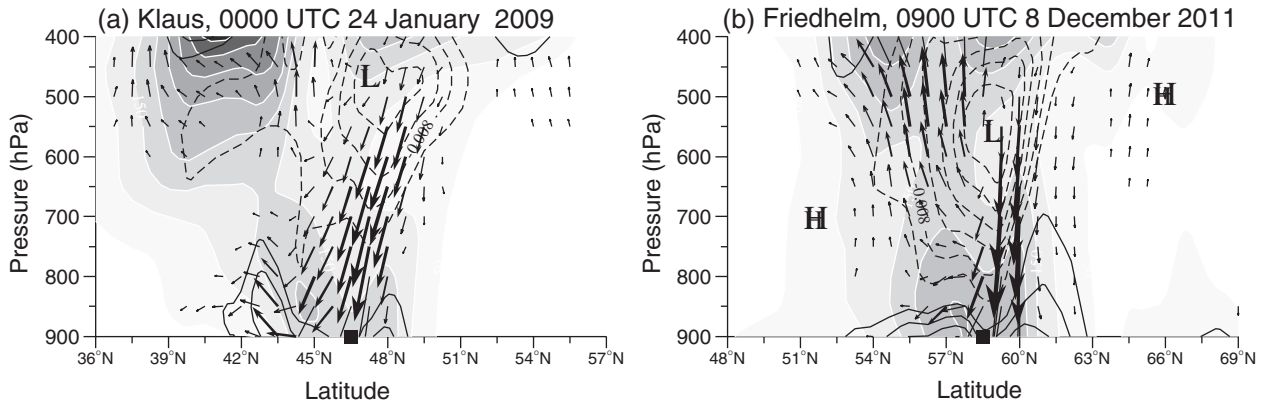

Figure 7. Vertical cross-section of the eddy kinetic energy (shadings with interval $50\,m^2s^{-2}$), convergence of the ageostrophic geopotential fluxes (black contours; dashed and solid for negative and positive values respectively, with interval $4\times10^{-3}m^2s^{-3}$) and ageostrophic geopotential fluxes (black arrows) for (a) *Klaus* and (b) *Friedhelm*. All the quantities have been longitudinally averaged between −1000 and +1000 km around the minimum high-frequency geopotential at 900 hPa. The black diamond denotes the latitude of the minimum high-frequency geopotential at 900 hPa at the time of interest.

the increase in EKE to the northwest of the cyclone centre is attributed to the sum of the advection and the Reynolds stress term. But later again at the beginning of the seclusion stage, the EKE increase to the southwest is clearly dominated by the positive pressure work which itself is due to the horizontal EKE redistribution orchestrated by the ageostrophic geopotential fluxes. Some differences between *Klaus* and *Friedhelm* are also noticeable. For *Friedhelm*, the wrapping of EKE occurs more or less at the same time as the rapid deepening of the surface cyclone which was not the case with *Klaus* for which the wrapping of EKE occurred 12 h after the rapid EKE growth. According to these two cases and supported by the idealized cyclones of RAJ14, the cyclonic wrapping of EKE occurred as soon as the surface cyclone lay on the cyclonic side of the jet, while the rapid deepening seems to depend more on the timing of the interaction with the upper-level trough.

The southwestward EKE redistribution set up by the horizontal ageostrophic geopotential fluxes at the beginning of the seclusion stage is accompanied by a downward EKE redistribution from mid- to very-low troposphere, as shown in Figure 7. The longitudinal average of the convergence of the total (i.e horizontal and vertical) ageostrophic geopotential fluxes is shown in black contours and the fluxes are represented by arrows. Regions of strong divergence of the fluxes are around 400–500 hPa for *Klaus* (Figure 7(a)) and at 500–600 hPa for *Friedhelm* (Figure 7(b)) and regions of convergence are localized below 800 hPa in both cases. The main part of the fluxes at that time are oriented downwards from mid-levels and then oriented southwards as they attain the low levels. Another part of the fluxes located in mid-troposphere south of the low center are oriented upwards toward the upper troposphere and is more significant for *Friedhelm*.

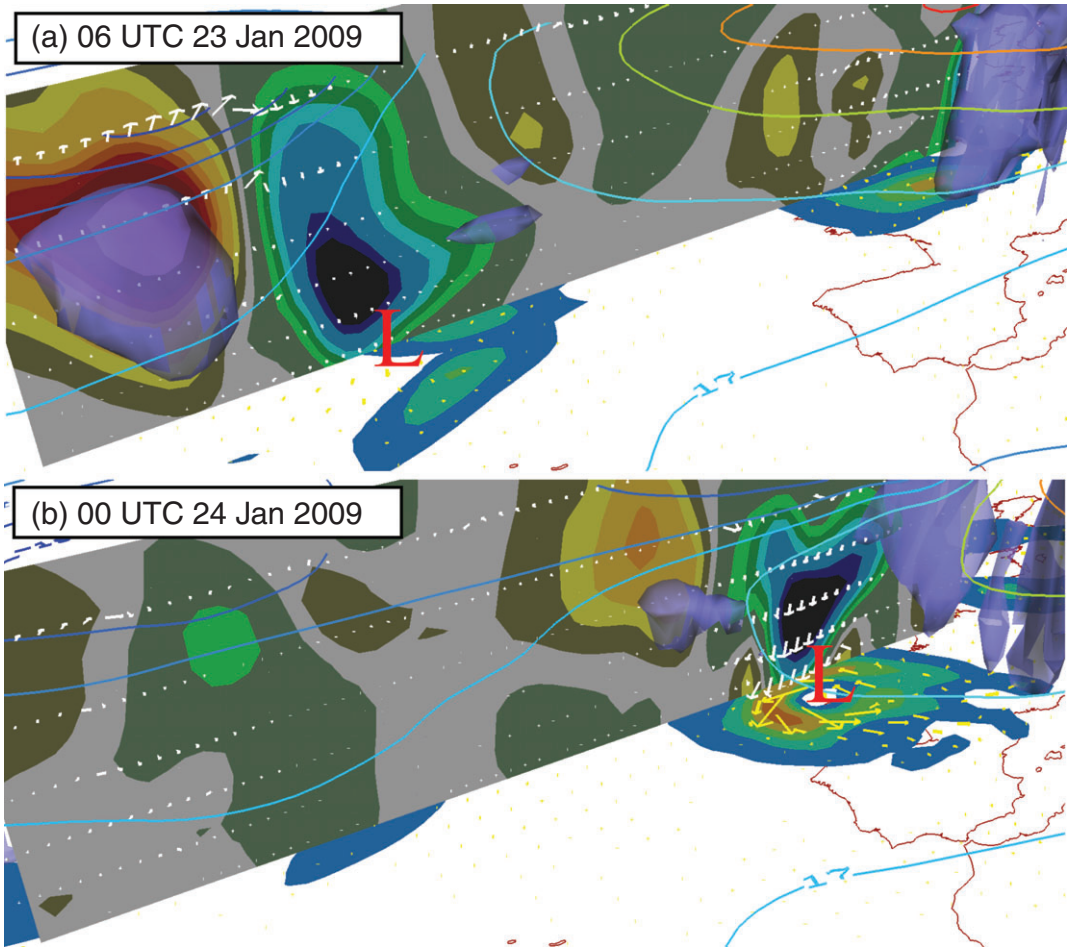

Figure 8. A three-dimensional view of the ageostrophic geopotential fluxes for *Klaus* at (a) 1200 UTC on 23 January and (b) 0000 UTC on 24 January. The blue semi-transparent shadings denote values of baroclinic conversion CI greater than 0.04 m^2s^{-3}. In the vertical cross-section, the vertical component of the ageostrophic fluxes is shown (with interval 100 Pa m^2s^{-3}, with blue and red shadings for downward and upward fluxes respectively), with the ageostrophic fluxes as white arrows. The colour contours denote the high-frequency geopotential Φ' at 300 hPa (with interval 500 m^2s^{-2}, with blue and red for negative and positive values respectively). On the horizontal plane at 850 hPa are shown EKE (shadings with interval 150 m^2s^{-2} for values greater than 150 m^2s^{-2}) and the horizontal ageostrophic fluxes $\Phi'\mathbf{u}'_a$ (yellow arrows).

Figures 8 and 9 complete the previous picture and offer a three-dimensional view of the ageostrophic geopotential fluxes at different stages for the two storms. At an early stage, large amplitudes of the fluxes are found in the upper troposphere (Figures 8(a) and 9(a)). They are upward oriented from a mid-tropospheric region where there is a local maximum of CI (clearly visible by the blue semi-transparent volume of CI shown in Figure 8(a)). This region corresponds to the descending motions located upstream of the upper trough (blue contours). More downstream in the upper troposphere near the centre of the upper trough, fluxes are downstream oriented corresponding to the so-called downstream development (Orlanski and Katzfey, 1991; Chang and Orlanski, 1993; Orlanski and Sheldon, 1995). Further downstream, the fluxes are downward oriented in regions of ascending motions. At the initiation stage, the lower-tropospheric fluxes are rather weak, as already mentioned. Despite these common features, *Klaus* and *Friedhelm* also present some differences. For instance, CI has its highest values upstream of the upper trough for *Klaus* and downstream of the low-level cyclone for *Friedhelm*. During the seclusion stage (Figures 8(b) and 9(b)), the highest values of CI are downstream of the low-level cyclone in the middle and lower troposphere for both cyclones, corresponding to ascending motions which occur in the northeastern quadrant of the cyclone (also Figures 5(c) and 6(c)). From those regions, the fluxes are downward oriented (white arrows in Figures 8(b) and 9(b)) on the northern flank of the cyclone, which is consistent with Figure 7. At 850 hPa, fluxes have their largest amplitudes on the western side of the cyclone where they redistribute EKE from the north to the south.

The three-dimensional picture of the fluxes as a function of time can be summarized as follows. At the early stage, the upward transfer on the western side is large but diminishes afterwards while the downward transfer on the eastern side becomes more important much later on, and is related to a strong downward redistribution from the mid- to the very-low troposphere. At this later stage, EKE is primarily formed by baroclinic conversion from eddy potential to EKE in the mid-troposphere to the northeast of the cyclone centre, but is redistributed downwards into the lower troposphere by the vertical ageostrophic geopotential fluxes before being rearward and cyclonically redistributed by the horizontal ageostrophic geopotential fluxes in the lower troposphere. These two real case-studies confirm the key role played by the three-dimensional ageostrophic fluxes in the formation of the low-level jet to the south of the cyclone centre which was found in a very idealized quasi-geostrophic model by RAJ14 and in a numerical weather prediction model by Papritz and Schemm (2013).

4. Conclusion and discussion

The formation of strong wind regions within two real winter windstorms crossing the low-frequency jet axis from its warm-air to its cold-air side has been analyzed using ERA-Interim data and an EKE budget. The different results are interpreted in the light of those obtained in the more idealized companion study of RAJ14. The different stages undergone by the present real storms closely follow those undergone by an idealized cyclone crossing a zonal jet in the two-layer quasi-geostrophic model. During the evolution of the storms, the location of the total

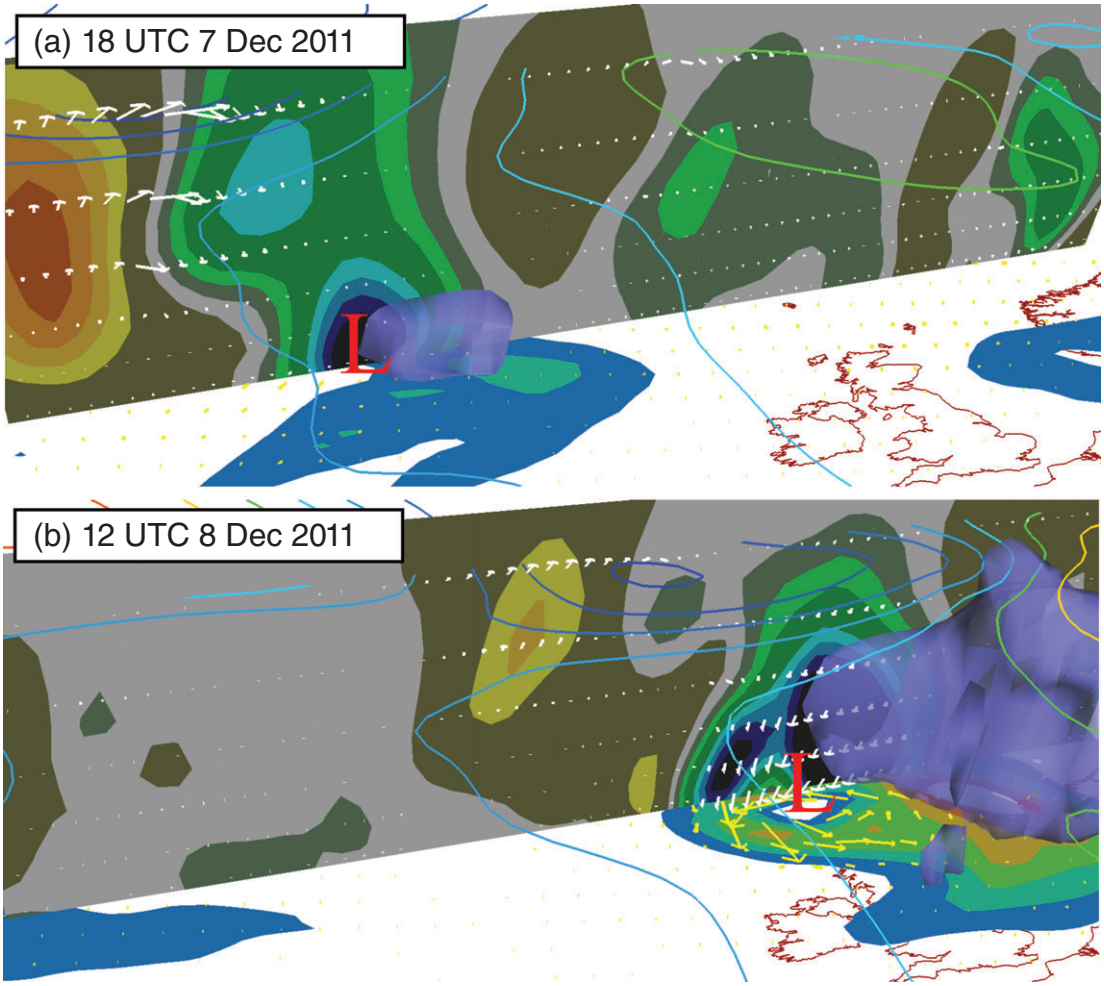

Figure 9. As Figure 8, but for *Friedhelm* at (a) 1800 UTC on 7 December and (b) 1200 UTC on 8 December.

wind speed maxima is explained by identifying regions where the high-frequency (eddy) winds have large amplitudes and combine favourably with the low-frequency (mean) winds. The transient low-level jets that appear around the cyclone centre can be thus interpreted by analyzing the EKE evolution. The main results are summarized below and lead to the conceptual model of Figure 10.

As long as the surface cyclone travels on the warm-air side (or anticyclonic side) of the mean jet, its shape is elongated southwest–northeast and the more intense low-level wind speeds are in the warm sector ahead of the cold front to the south of the cyclone centre. The maximum wind speed is reached in that region because the eddy winds have large amplitudes to the southeast of the cyclone where they are southwest–northeast oriented and form an acute angle with the eastward-oriented mean winds (stage I of Figure 10). An interpretation of this particular feature of EKE distribution when the cyclone moves on the anticyclonic side of the jet was provided by RAJ14 within an idealized quasi-geostrophic framework. The anticyclonically sheared environment added to the strong vertically averaged potential vorticity gradient due to the presence of a westerly jet diminishes the eastward ageostrophic wind and the westward ageostrophic geopotential fluxes in the lower troposphere, preventing the rearward and cyclonic redistribution of EKE. This interpretation has been confirmed in the present real case-studies as the ageostrophic geopotential fluxes were found to be weak in the lower troposphere before the crossing of the jet (Figure 8(a)). In the upper troposphere, the intense eastward-oriented fluxes are characteristic of the so-called downstream development (Orlanski and Sheldon, 1995).

When the surface cyclone is moving to the jet-core region, EKE begins to be cyclonically redistributed and large values of EKE are already found on the northern flank of the cyclone (stage II of Figure 10). There are still strong EKE maxima ahead of the cold front but, the eddy winds being more northward oriented, they combine less favourably with the mean westerlies. At this intermediate stage, high total wind speeds are found ahead of and behind the cold front. The maximum wind speed can be reached in one of the two previous regions. If it occurs ahead of the cold front as in the schematic of Figure 10, it is because the eddy winds are still strong enough there (Figure 3(f)). If it occurs behind the cold front, it is because the eddy winds align with the mean westerlies (Figure 2(h)). During that particular stage, the sum of the advection and of the Reynolds stress terms participates in the cyclonic displacement of the EKE maximum located on the northern flank of the cyclone (Figure 4(e)). The lower-tropospheric ageostrophic geopotential fluxes are still rather weak at that time (Figure 4(h)).

When the surface cyclone lies entirely on the cold-air side (or cyclonic side) of the mean jet, the bent-back warm front stage occurs, the cyclone vorticity rapidly gets a comma shape, and the lower-tropospheric EKE is southwestward redistributed (stage III of Figure 10). Such a redistribution of EKE to the south creates intense eddy westerlies there, which add favourably to the mean westerlies to form a strong low-level westerly jet orthogonal to the cold front (Figures 2(j) and 3(h)), consistent with Grønas (1995)'s remark. It is the southwestward oriented ageostrophic geopotential fluxes that mainly contribute to the accumulation of EKE on the southwestern quadrant of the cyclone at the end of the bent-back warm front stage and the beginning of the seclusion stage (Figures 5(h) and 6(h)). The reason why ageostrophic geopotential fluxes are stronger and more efficient to rearwardly and cyclonically redistribute EKE when the cyclone evolves on the cyclonic side of the jet comes from the additional effects of the nonlinear and linear components of the irrotational ageostrophic wind (RAJ14). Nonlinear advection

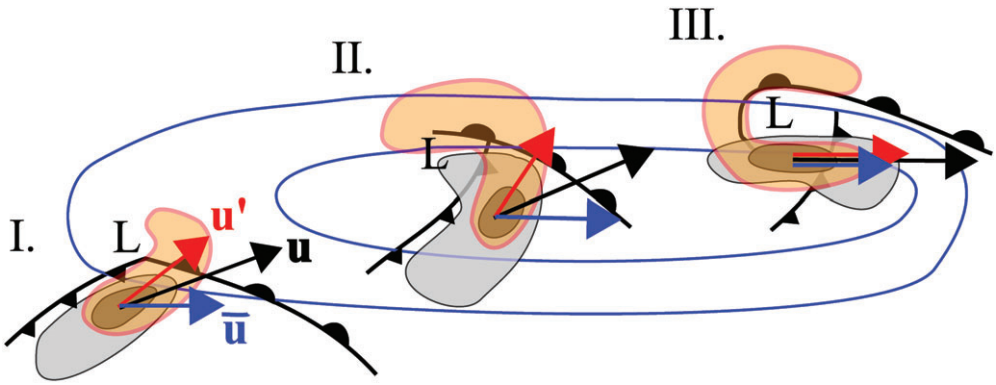

Figure 10. Schematic representation of the different stages of EKE redistribution undergone by jet-crossing cyclones following the conceptual model of Shapiro and Keyser (1990): (I) the incipient frontal cyclone, (II) the frontal fracture and (III) the T-bone and bent-back front stage. The blue contours denote the low-level low-frequency wind speed, i.e. the mean jet which is zonally oriented. The cold and warm fronts are in black, the total wind speed in grey shading, and the high-frequency wind speed in red shading. The high-frequency geopotential minimum is denoted by the letter L. The blue, red, and black arrows represent respectively the low-frequency, high-frequency and total velocity at the point of maximum wind speed (i.e. $\overline{\mathbf{u}}$, $\mathbf{u}'$ and $\mathbf{u}$).

also participates in the cyclonic EKE redistribution at that time but less importantly.

The three-dimensional picture of EKE redistribution at the later stage of the cyclones' evolution is as follows. The baroclinic conversion rate from eddy potential energy to EKE attains large values in the mid-troposphere to the northeast of the surface cyclone. This is the main term responsible for EKE generation, even though the direct baroclinic conversion from mean energy to EKE involved in the Reynolds stress term also participates somehow in EKE generation to the north of the cyclone. Vertical ageostrophic fluxes downwardly redistribute EKE from the region of EKE generation located to the northeast of the cyclone before being redistributed southwestwards by the horizontal ageostrophic fluxes and the nonlinear advection in the very-low troposphere. This confirms the recent numerical studies of Papritz and Schemm (2013) and RAJ14. It may come as a surprise that the formation of intense low-level jets in explosively deepening cyclones, associated with intense diabatic processes, closely follows scenarios of idealized dry simulations. However, it should be recalled that (i) all the computed dynamical terms of the present EKE budget indirectly take into account moist processes through the use of ERA-Interim datasets, and (ii) the mid-tropospheric heating rate generated by moist processes is not directly included in the EKE budget. Rather, the heating is directly involved in the eddy potential energy budget. In other words, without considering dissipative effects, the decomposition of the EKE budget is the same in dry and moist cases.

Despite the previously mentioned common features between both storms, differences have been also noticed. First, the large-scale jet was much wider in the *Klaus* case than in the *Friedhelm* case. Second, *Klaus* was initiated far south of the large-scale jet and *Friedhelm* much closer to its axis. Finally, the strongest deepening occurred during the jet-crossing phase for *Klaus* but much later for *Friedhelm*.

One originality of the present article is the interpretation of EKE redistribution acting in different parts of a given cyclone, while previous real case-studies have investigated energy redistribution from one cyclone to another (Orlanski and Katzfey, 1991; Orlanski and Sheldon, 1995). The same ageostrophic geopotential fluxes that are responsible for the so-called downstream development at upper levels are shown here to provide a dynamical interpretation for the low-level jet formation to the south of the cyclone centre. We believe that this constitutes favourable synoptic conditions for the existence of finer-scale jets such as sting jets (Browning, 2004). Further studies should investigate how this EKE redistribution at the synoptic scale may exert its influence at the mesoscale and may participate in the formation of the cold-conveyor-belt jet or sting jet. Another aspect to analyze would be the importance of the jet-crossing phase for the occurrence of such mesoscale jets.

Appendix

Examples of anticorrelation between the pressure work and advection terms

Let us present two simple examples where the pressure work and advection terms tend to cancel each other in the quasi-geostrophic barotropic context. The geostrophic wind is denoted as $\mathbf{u}$ in the present Appendix and is supposed to be the sum of a spatially uniform zonal basic flow $\overline{\mathbf{u}}$ and a perturbation $\mathbf{u}'$. In the quasi-geostrophic barotropic context, the perturbation ageostrophic wind has only a rotational part $\mathbf{u}'_{\mathrm{a}} = -(1/f_0)\mathbf{k} \wedge \nabla\phi'_{\mathrm{a}}$. Within such a framework, the perturbation momentum equations on a β-plane can be written as

$$\frac{\partial \mathbf{u}'}{\partial t} = -\overline{\mathbf{u}}\cdot\nabla\mathbf{u}' - \mathbf{u}'\cdot\nabla\mathbf{u}' - \nabla\phi'_{\mathrm{a}} + \beta y \nabla\psi', \qquad \text{(A1)}$$

where $\psi' = \Phi'/f_0$ is the perturbation geostrophic streamfunction, f_0 the uniform Coriolis parameter and β the planetary vorticity gradient. By adding the phase-shift tendency $\mathbf{c}\cdot\nabla\mathbf{u}'$ to Eq. (A1) and multiplying the result by $\mathbf{u}'$, one can find the EKE equation

$$\left(\frac{\partial}{\partial t} + \mathbf{c}\cdot\nabla\right) K' = (\mathbf{c} - \overline{\mathbf{u}})\cdot\nabla K' - \mathbf{u}'\cdot\nabla K' - \mathbf{u}'\cdot\left(\nabla\phi'_{\mathrm{a}} - \beta y\nabla\psi'\right), \qquad \text{(A2)}$$

which can be also expressed as

$$\left(\frac{\partial}{\partial t} + \mathbf{c}\cdot\nabla\right) K' = (\mathbf{c} - \overline{\mathbf{u}})\cdot\nabla K' - \mathbf{u}'\cdot\nabla K' - \left(\mathbf{u}'_{\mathrm{a}} + \frac{\beta y}{f_0}\mathbf{u}'\right)\cdot\nabla\Phi'. \qquad \text{(A3)}$$

The divergence of Eq. (A1) leads to

$$\nabla^2\phi'_{\mathrm{a}} = 2J(u', v') + \nabla\cdot\left(\beta y\nabla\psi'\right), \qquad \text{(A4)}$$

where J is the Jacobian operator. The previous diagnostic equation allows us to determine the ageostrophic wind from the sole knowledge of the geostrophic wind at each given time.

A first simple case to be considered is the canonical case of linear Rossby wave propagation. In such a case, by supposing the perturbation of monochromatic shape

$$\psi' \propto e^{im(x-ct)},$$

one can find from Eq. (A4) that $\phi'_{\mathrm{a}} = \beta y\psi'$ and $\mathbf{u}'_{\mathrm{a}} + (\beta y/f_0)\mathbf{u}' = (\beta\psi'/f_0)\mathbf{i}$, where $\mathbf{i}$ is the zonal unit vector.

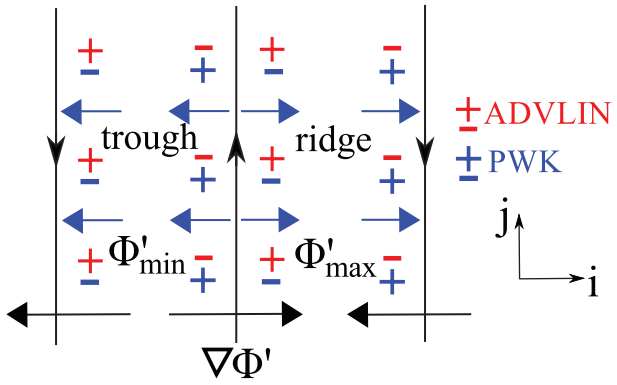

Figure A1. Schematic showing EKE tendencies for a monochromatic Rossby wave on a β-plane. The vertical black lines represent contours of the perturbation geopotential, the black arrows the gradient of the perturbation geopotential, and the blue arrows the ageostrophic wind $\mathbf{u}'_a + (\beta y/f_0)\mathbf{u}'_g$. The + and − signs denote positive and negative EKE tendencies respectively, in red those of the linear advection term ADVLIN $= (\mathbf{c} - \overline{\mathbf{u}})\cdot\nabla K'$ and in blue those of the pressure work PWK $= -\mathbf{u}'_a\cdot\nabla\Phi'$.

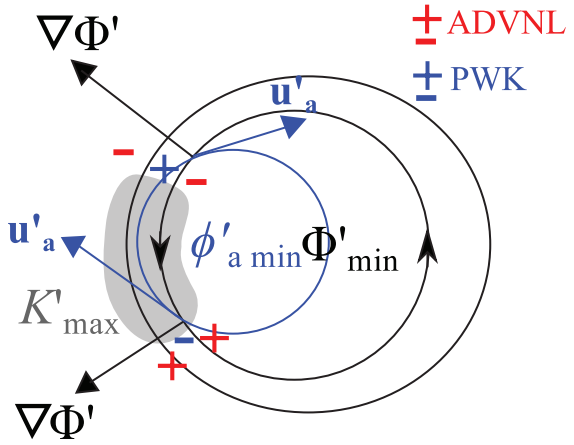

Figure A2. Schematic showing EKE tendencies for an isolated cyclone on an f-plane having an EKE maximum on its western flank (area with grey shading). The blue line represents a contour of ϕ'_a. The red + and − signs denote positive and negative values respectively of the nonlinear advection term ADVNL $= -\mathbf{u}'\cdot\nabla K'$. All other definitions are as in Figure A1.

The ageostrophic wind $\mathbf{u}'_a + (\beta y f_0)\mathbf{u}'$ is westward oriented in the trough region and eastward oriented in the ridge region (Figure A1). The pressure work $-\left\{\mathbf{u}'_a + (\beta y/f_0)\mathbf{u}'\right\}\cdot\nabla\Phi'$ is thus positive and negative on the eastern and western sides of the geopotential anomalies and is entirely compensated by the linear advection term $(\mathbf{c} - \overline{\mathbf{u}})\cdot\nabla K'$. Indeed, the net EKE tendency is zero in Eq. (A3) because we consider monochromatic perturbations having real phase speeds. There is no redistribution of EKE in the trough and ridge frame. In such a case, the first and second terms of the equation are non-zero and entirely compensate each other.

A second and less trivial case of compensation between the pressure work and the advection terms is shown in Figure A2. The flow is now supposed to evolve on an f-plane, there is no basic flow, and the perturbation has a finite amplitude taking the shape of a cyclonic vortex with an EKE maximum on its western flank. Nonlinear advection $-\mathbf{u}'\cdot\nabla K'$ acts to cyclonically rotate the EKE maximum (the red + and − signs). On the other hand, the pressure work has the reverse tendencies (the blue + and − signs) which can be anticipated by analyzing Eq. (A4) and noting that ϕ'_a has a minimum to the west of the Φ' minimum. We conclude that the pressure work $-\mathbf{u}'_a\cdot\nabla\Phi'$ tends to anticyclonically displace the EKE maximum and has therefore the opposite effect to nonlinear advection (Figure A2). To get an idea of the net effect, Eq. (A4) can be approximated in the vicinity of the EKE maximum by

$$\nabla^2\phi'_a \simeq -2\partial_x v'\partial_y u'.$$

The order of magnitude of ϕ'_a is thus approximately

$$2\frac{1}{L_x^2}\frac{1}{L_y^2}\psi'^2 \Big/ \left(\frac{1}{L_x^2} + \frac{1}{L_y^2}\right),$$

where L_x and L_y represent the order of magnitude of the zonal and meridional scales respectively. The order of magnitude of K' being

$$\frac{1}{2}\left(\frac{1}{L_x^2} + \frac{1}{L_y^2}\right)\psi'^2,$$

one can easily deduce that ϕ'_a is smaller in amplitude than K' and PWK $= -\mathbf{u}'\cdot\nabla\phi'_a$ is smaller than ADVNL $= -\mathbf{u}'\cdot\nabla K'$. Therefore, the cyclonic redistribution of EKE by nonlinear advection generally overwhelms the anticyclonic redistribution by the pressure work and one can expect that the net effect is a cyclonic redistribution of EKE. In the baroclinic context, this partial compensation was diagnosed in RAJ14 between the nonlinear advection and the pressure work component induced by the rotational ageostrophic wind (their Figure 6(i,k)). This may partly explain why in many regions nonlinear advection and the pressure work have opposite signs. However, it should be mentioned that the pressure work component due to the irrotational ageostrophic wind is mainly responsible for the rearward and cyclonic redistribution of EKE as shown by RAJ14. This particular component of the pressure work tends to have the same effect as nonlinear advection and may explain why there are also regions where the pressure work and nonlinear advection have the same signs, such as on the southwestern flank of the cyclone (Figure 5(h, i)).

Acknowledgements

The authors would like to thank Heini Wernli and an anonymous reviewer for their suggestions which helped to improve the clarity and conciseness of the article. Jean Maziejewski is also sincerely acknowledged for proofreading an early version of the manuscript.

References

Baker L, Martinez-Alvarado O, Methven J, Knippertz P. 2013. Flying through extratropical cyclone Friedhelm. *Weather* **68**: 9–13.

Baker LH, Gray SL, Clark PA. 2014. Idealised simulations of sting-jet cyclones. *Q. J. R. Meteorol. Soc.* **140**: 96–110.

Browning KA. 2004. The sting at the end of the tail: Damaging winds associated with extratropical cyclones. *Q. J. R. Meteorol. Soc.* **130**: 375–399.

Browning KA, Pardoe CW. 1973. Structure of low-level jet streams ahead of mid-latitude cold fronts. *Q. J. R. Meteorol. Soc.* **99**: 619–638.

Carlson TN. 1980. Airflow through midlatitude cyclones and the comma cloud pattern. *Mon. Weather Rev.* **108**: 1498–1509.

Chang EKM, Orlanski I. 1993. On the dynamics of a storm track. *J. Atmos. Sci.* **50**: 999–1015.

Clark PA, Browning KA, Wang C. 2005. The sting at the end of the tail: Model diagnostics of fine-scale three-dimensional structure of the cloud head. *Q. J. R. Meteorol. Soc.* **131**: 2263–2292.

Davies HC, Schär C, Wernli H. 1991. The palette of fronts and cyclones within a baroclinic wave development. *J. Atmos. Sci.* **48**: 1666–1689.

Dee DP, Uppala SM, Simmons AJ, Berrisford P, Poli P, Kobayashi S, Andrae U, Balmaseda MA, Balsamo G, Bauer P, Bechtold P, Beljaars ACM, van de Berg L, Bidlot J, Bormann N, Delsol C, Dragani R, Fuentes M, Geer AJ, Haimberger L, Healy SB, Hersbach H, Hólm EV, Isaksen L, Kållberg P, Köhler M, Matricardi M, McNally AP, Monge-Sanz BM, Morcrette J-J, Park B-K, Peubey C, de Rosnay P, Tavolato C, Thépaut J-N, Vitart F. 2011. The ERA-Interim reanalysis: Configuration and performance of the data assimilation system. *Q. J. R. Meteorol. Soc.* **137**: 553–597.

Gilet J-B, Plu M, Rivière G. 2009. Nonlinear baroclinic dynamics of surface cyclones crossing a zonal jet. *J. Atmos. Sci.* **66**: 3021–3041.

Gray SL, Martinez-Alvarado O, Baker LH, Clark PA. 2011. Conditional symmetric instability in sting-jet storms. *Q. J. R. Meteorol. Soc.* **137**: 1482–1500.

Grønas S. 1995. The seclusion intensification of the New Year's day storm 1992. *Tellus* **47A**: 733–746.

Harrold TW. 1973. Mechanisms influencing the distribution of precipitation within baroclinic disturbances. *Q. J. R. Meteorol. Soc.* **99**: 232–251.

Lackmann GM. 2002. Cold-frontal potential vorticity maxima, the low-level jet, and moisture transport in extratropical cyclones. *Mon. Weather Rev.* **130**: 59–74.

Lackmann GM, Keyser D, Bosart LF. 1999. Energetics of an intensifying jet streak during the experiment on rapidly intensifying cyclones over the Atlantic (ERICA). *Mon. Weather Rev.* **127**: 2777–2795.

Liberato MRL, Pinto JG, Trigo IF, Trigo RM. 2011. Klaus–an exceptional winter storm over northern Iberia and southern France. *Weather* **66**: 330–334.

Lim GH, Holton JR, Wallace JM. 1991. The structure of the ageostrophic wind field in baroclinic waves. *J. Atmos. Sci.* **48**: 1733–1745.

Martínez-Alvarado O, Gray SL, Catto JL, Clark PA. 2012. Sting jets in intense winter North Atlantic windstorms. *Environ. Res. Lett.* **7**: 024014, doi: 10.1088/1748-9326/7/2/024014.

Martínez-Alvarado O, Baker LH, Gray SL, Methven J, Plant RS. 2014. Distinguishing the cold conveyor belt and sting jet air streams in an intense extratropical cyclone. *Mon. Weather Rev.*, doi: 10.1175/MWR-D-13-00348.1.

Neiman PJ, Shapiro MA, Fedor LS. 1993. The life cycle of an extratropical marine cyclone. Part II: Mesoscale structure and diagnostics. *Mon. Weather Rev.* **121**: 2177–2199.

Nielsen NW, Sass BH. 2003. A numerical, high-resolution study of the life cycle of the severe storm over Denmark on 3 December 1999. *Tellus* **55A**: 338–351.

Orlanski I, Katzfey J. 1991. The life cycle of a cyclone wave in the Southern Hemisphere. Part I: Eddy energy budget. *J. Atmos. Sci.* **48**: 1972–1998.

Orlanski I, Sheldon JP. 1995. Stages in the energetics of baroclinic systems. *Tellus* **47A**: 605–628.

Papritz L, Schemm S. 2013. Development of an idealised downstream cyclone: Eulerian and Lagrangian perspective on the kinetic energy. *Tellus* **65A**: 19539, doi: 10.3402/tellusa.v65i0.19539.

Petterssen S, Smebye SJ. 1971. On the development of extratropical cyclones. *Q. J. R. Meteorol. Soc.* **97**: 457–482.

Rivière G, Joly A. 2006. Role of the low-frequency deformation field on the explosive growth of extropical cyclones at the jet exit. Part I: Barotropic critical region. *J. Atmos. Sci.* **63**: 1965–1981.

Rivière G, Arbogast P, Lapeyre G, Maynard K. 2012. A potential vorticity perspective on the motion of a mid-latitude winter storm. *Geophys. Res. Lett.* **39**: L12808, doi: 10.1029/2012GL052440.

Rivière G, Gilet J-B, Oruba L. 2013. Understanding the regeneration stage undergone by surface cyclones crossing a mid-latitude jet in a two-layer model. *J. Atmos. Sci.* **70**: 2832–2853.

Rivière G, Arbogast P, Joly A. 2014. Eddy kinetic energy redistribution within idealized extratropical cyclones using a two-layer quasi-geostrophic model. *Q. J. R. Meteorol. Soc.*, doi: 10.1002/qj.2350.

Rossa AM, Wernli H, Davies HC. 2000. Growth and decay of an extratropical cyclone's PV-tower. *Meteorol. Atmos. Phys.* **73**: 139–156.

Sanders F, Gyakum JR. 1980. Synoptic-dynamic climatology of the 'bomb'. *Mon. Weather Rev.* **108**: 1589–1606.

Schultz DM. 2001. Re-examining the cold conveyor belt. *Mon. Weather Rev.* **129**: 2205–2225.

Schultz DM, Sienkiewicz JM. 2013. Using frontogenesis to identify sting jets in extratropical cyclones. *Weather and Forecasting* **28**: 603–613.

Schultz DM, Keyser D, Bosart LF. 1998. The effect of large-scale flow on low-level frontal structure and evolution in midlatitude cyclones. *Mon. Weather Rev.* **126**: 1767–1791.

Shapiro MA, Keyser D. 1990. Fronts, jet streams and the tropopause. In *Extratropical Cyclones: The Erik Palmén Memorial Volume*, Newton CW, Holopainen EO.(eds.): 167–191. American Meteorological Society: Boston, MA.

Smart DJ, Browning KA. 2013. Attribution of strong winds to a cold conveyor belt and sting jet. *Q. J. R. Meteorol. Soc.* **140**: 595–610.

Vaughan G, Methven J, Anderson D, Antonescu B, Baker L, Baker TP, Ballard SP, Bower KN, Brown PRA, Chagnon J, Choularton J, Chylik PJ, Connolly TW, Cook PA, Cotton RJ, Crosier J, Dearden C, Dorsey JR, Frame THA, Gallagher MW, Goodliff M, Harvey BJ, Gray SL, Knippertz P, Lean HW, Li D, Lloyd G, Martinez-Alvarado O, Nicol J, Norris J, Öström E, Owen J, Parker DJ, Plant RS, Renfrew IA, Roberts NM, Rosenberg P, Rudd AC, Schultz DM, Taylor JP, Trzeciak T, Tubbs R, Vance AK, van Leeuwen PJ, Wellpott A, Woolley A. 2014. Cloud banding and winds in intense European cyclones –Results from the DIAMET Project. *Bull. Am. Meteorol. Soc.* In Press.

Wernli H. 1997. A Lagrangian-based analysis of extratropical cyclones. Part II: A detailed case-study. *Q. J. R. Meteorol. Soc.* **123**: 1677–1706.

Wernli H, Fehlmann R, Luthi D. 1998. The effect of barotropic shear on upper-level induced cyclogenesis: Semi-geostrophic and primitive equation numerical simulations. *J. Atmos. Sci.* **55**: 2080–2094.

